



Thousandfold boosting instantaneous current of triboelectric nanogenerator based on decoupled charge pump and discharge tube[☆]

Ze Yang^{a,b,1}, Yiyong Yang^{a,*,1}, Fan Liu^{b,d,1}, Bo Li^a, Yinbo Li^b, Xu Liu^b, Jiaqi Chen^a, Chengbiao Wang^a, Linhong Ji^b, Zhong Lin Wang^{c,e,**}, Jia Cheng^{b,*}

^a School of Engineering and Technology, China University of Geosciences (Beijing), Beijing 100083, PR China

^b State Key Laboratory of Tribology, Department of Mechanical Engineering, Tsinghua University, Beijing 100084, PR China

^c Beijing Institute of Nanoenergy and Nanosystems, Chinese Academy of Sciences, Beijing 100083, PR China

^d Department of Mechanical Engineering, Massachusetts Institute of Technology, Cambridge, MA 02139, United States

^e School of Materials Science and Engineering, Georgia Institute of Technology, Atlanta, GA 30332, United States

ARTICLE INFO

Keywords:

Decoupled charge pump
Triboelectric nanogenerator
Charge density
Current boost
Discharge tube

ABSTRACT

The triboelectric nanogenerators (TENGs) are facing great challenges of high power and long life in practical applications, owing to low charge density, easy wear material, etc. Trying to address those limitations, a new operation method of decoupled charge pump for TENG along with the discharge tube is proposed to thousandfold improve its instantaneous peak current. The pump and main TENGs optimally adopt the freestanding mode and contact-separation mode, respectively, and their motions are decoupled. When the capacitance of the main TENG as a variable capacitor reaches the peak value, there is the maximum charge generation from pump TENG and charge injection into main TENG. With the integration of discharge tube, the output current has an above 1000 folds increase and the power density is calculated to 21.25 W/m². A charge density of 628.7 μC m⁻² is achieved. This work provides a new mode of charge pump with intermittent operation for enormously boosting the output current of TENGs, promoting its practical applications.

1. Introduction

In the new era of Internet-of-Things (IoT) and 5 G [1], portable and wearable electronics, distributed sensor network, and mobile information monitoring microsystem are indispensable for making people's life happier and healthier [2–4]. Accordingly, the distributed and low-watt energy sources for powering those electronics are the keys. Currently, the lithium battery is still widely and mostly used as the energy source [5]. However, what should not be ignored are that the batteries have limited lifetimes and capacities, and the frequent replacement and recharging of them is also a big challenge, especially when they are tiny, widely distributed and with huge number of units [6,7]. Meanwhile, their recycling and harmless treatment are also tough tasks. Therefore, much effort has been devoted to developing and exploring new energy

sources as the complement or replacement of batteries [8,9]. Among them, the triboelectric nanogenerator [10–12] (TENG) has drawn much attention owing to its merits of low cost, various materials and effectiveness for low-frequency energy harvesting, demonstrating a great potential toward the clear energy for self-powered systems [13–17].

Since invented in 2012 [18], the TENG, based on the coupling effect of triboelectrification and electrostatic induction [19], has witnessed enormous progress and achievements in micro-nano energy [20–23], self-powered sensing [24–29], blue energy harvesting [30–32], and high voltage applications [33–36]. Nevertheless, the TENGs are facing great challenges of high power and long life in practical applications because of low charge density, easy wear material, etc.

As for the wear problem, some researchers utilized the lubricants sprayed on the interface of materials to lower abrasion [37] and some

[☆] “Prof Zhong Lin Wang, an author on this paper, is the Editor-in-Chief of Nano Energy, but he had no involvement in the peer review process used to assess this work submitted to Nano Energy. This paper was assessed, and the corresponding peer review managed by Professor Chenguo Hu, also an Associate Editor in Nano Energy”.

* Corresponding authors.

** Correspondence to: Beijing Institute of Nanoenergy and Nanosystems, Chinese Academy of Sciences.

E-mail addresses: yangyy@cugb.edu.cn (Y. Yang), zhong.wang@mse.gatech.edu (Z.L. Wang), chengjia@tsinghua.edu.cn (J. Cheng).

¹ Z.Y., Y.Y. and F.L. contributed equally to this work.

ones directly used floating materials without contact between them [38]. Those methods are effective and the works are quite outstanding. For the second limitation, the traditional methods that have improved the charge density from $240 \mu\text{C m}^{-2}$ to $1003 \mu\text{C m}^{-2}$ are focused on the material selection, chemical modification, structure optimization, and environment control [39,40]. Much effort has been devoted to addressing the two key issues and great progress has been made by the forerunners, which is admirable and beneficial to the followers.

Recently, the emerging charge pumping technologies have broken the bottleneck of charge density enhancement from the ultrahigh $1020 \mu\text{C m}^{-2}$ to the maximum of $1850 \mu\text{C m}^{-2}$, such as the charge pump with a separated conductive layer in 2018 [41], the self-charge excitation system with a voltage-multiplying circuit in 2019 [42], the contact-separated charge pump with shuttling charges in 2020 [43], and the sliding charge pump with a switch circuit in 2021 [44], etc. Those works are also excellent and indeed deserve a storm of sustained applause, and they should be studied and further advanced. To enhance the output performance of TENG, there may be other method and strategy for the reference.

In this work, a new operation method of decoupled charge pump for TENG (DCP-TENG) along with the discharge tube is demonstrated to thousandfold improve the instantaneous peak current of TENG. The DCP-TENG, for the first time, adopts hybrid rotary freestanding triboelectric-layer and vertical contact-separation modes as pump and main TENGs respectively and innovatively decouples their synchronous motions, maximizing the charge injection and storage when the capacitance of main TENG reaches the peak value. Two dielectrics have an intermittent close contact and friction for the charging, reducing the material abrasion [45–47]. In addition, a voltage booster circuit (VBC) is utilized to elevate and rectify the input voltage and a buffer capacitor (BFC) for storing charges. With the discharge tubes (DTs) like the reported works [48,49], the output current has an above 1000 folds increase from $59.2 \mu\text{A}$ to 69.1 mA and the average power is calculated to 2.43 W , achieving a power density of 21.25 W/m^2 . Meanwhile, a charge density of $628.7 \mu\text{C m}^{-2}$ is obtained within this DCP-TENG. The output is high enough to power 936 small light-emitting diodes (LEDs) with a diameter of 5 mm, 454 big LEDs of 10 mm, three high-voltage ultraviolet tubes, and the low-watt electronic calculator, watches and sensors, etc. This work could shield a new light on high-performance energy harvesting approach for TENG to its practical applications.

2. Results and discussion

2.1. Device structure and working principle of DCP-TENG

As shown in Fig. 1a, the DCP-TENG is mainly composed of three parts, namely the motion input unit with a servo motor, the motion transferring unit and the electricity generation unit. Driving motion from the servo motor is divided into a rotation of the rotator within pump TENG and a contact-separation movement of two electrodes within main TENG.

A buffer capacitor (BFC) is in series with main TENG to store extra charges and distribute accordingly. The power management unit (PMU) is used to rectify and maintain the input voltage from pump TENG, while the changeable voltage on BFC is to drive a discharge tube (DT) for the electricity output. Fig. 1b is the real product of electricity generation unit without the rotor, and the other key components are presented in Fig. S1. As described in Fig. 1c, the thimble fixed on a rotating shaft and the petaloid cam can collaboratively realize the contact-separation movement of two electrodes within main TENG, while the relative rotation of cam two to cam one is for the intermittent close contact of two dielectrics within pump TENG. The cam two and cam base can be connected to be an integrated cam owing to their specially designed structures and the petaloid cam can move forward and backward within its cavity. The length of thimble is shorter than the inner diameter of

cam two for the motion-free interference.

One part of Fig. 1d shows the structure of electricity generation unit in detail. The thimble and the rotor are both fixed on a rotating shaft with a synchronous rotation, while cam base and petaloid cam are on the stator and half substrate of main TENG respectively. The front and back supports are connected by three screws with three compressive springs, so are the stator and the main TENG. The stator is fixed on the screws between two supports. Detailed movement description is explained in Fig. S2.

The Fig. 1d also demonstrates the structure of motion transferring unit (Fig. S3). The driving motion from a servo motor is transmitted to the shaft through two couplers and a synchronous belt wheel, and to the cam one through a gear reducer and the other synchronous belt wheel. A composite bearing consisting of three bearings of small, medium, and big sizes, makes it possible for the cam one and the shaft to have different rotating speeds. The cam one has a rotation while the cam two has a horizontal movement along with the shaft. As a result, the rotor has a faster rotation while the nylon film adhered on the stator has a slower contact-separation movement with polyvinyl chloride (PVC) film, achieving an intermittent close contact and friction within two dielectrics. The whole structure of DCP-TENG is described in Fig. S4 and Video S1.

Supplementary material related to this article can be found online at [doi:10.1016/j.nanoen.2022.107264](https://doi.org/10.1016/j.nanoen.2022.107264).

To better understand the work process of DCP-TENG, an analogical mode based on a hydropower turbine is described in Fig. 1e. This mode presents two connected vessels as an integrated communicating vessel and a hydropower turbine. One vessel has a variable capacity adjusted by a moving plunger while the other one has a fixed capacity, corresponding to the main TENG and the BFC, respectively. Connected to the right vessel, the hydropower turbine works as the external load to convert the fluid flowing energy into the rotation energy and outputs power when the inside valve is open for the flowing out of medium. The open of control valve by the floater depends on the water level and potential, which is in analogy with the fact that the terminal potential of BFC controls the current conduction of the DT and the power output on loads.

In the storage phase (I), the fluid medium is injected into two vessels with the maximum but limited volume, leading to a low water level and potential and the resultant unopened state of control valve. In the release phase (II), the rightward movement of the plunger by an external agitation compresses the capacity of left vessel, lifting the water level and potential for the open of control valve. Therefore, there is much fluid medium flowing through the turbine for energy conversion and power output. Meanwhile, the high hydraulic pressure accelerates the flowing speed of medium, promoting the output efficiency. Accordingly, the injected charges by pump TENG works as the fluid medium, driven by the electric potential and outputting power on loads. The DT acts as the control valve for the faster and higher flow of charges and currents, promoting the power output. Moreover, the main TENG has the maximum capacitance for the charge storage and the pump TENG has a faster charge generation and injection when two dielectrics have the close contact and friction, also similar to the analogical mode.

The working principle of DCP-TENG is illustrated in Fig. 1f. The DCP-TENG adopts hybrid pump TENG in freestanding triboelectric-layer mode and main TENG in contact-separation mode. A VBC is utilized to provide a rectified and constant input voltage for main TENG and a BFC in series. Main TENG also serves as a variable capacitor with a contact-separation motion of its plate aluminum electrodes. Its equivalent capacitance and terminal open-circuit voltage are thus changeable, which results in a fluctuant voltage on BFC. When the voltage on BFC is higher than the breakdown voltage of DT, there is an electricity output and a current flowing through the load. Meanwhile, the Kapton and Polyethylene terephthalate (PET) films not only function as the tribo-layers but also separate metal electrodes from each other and the air. A Zener diode between two output terminals of VBC is adopted for

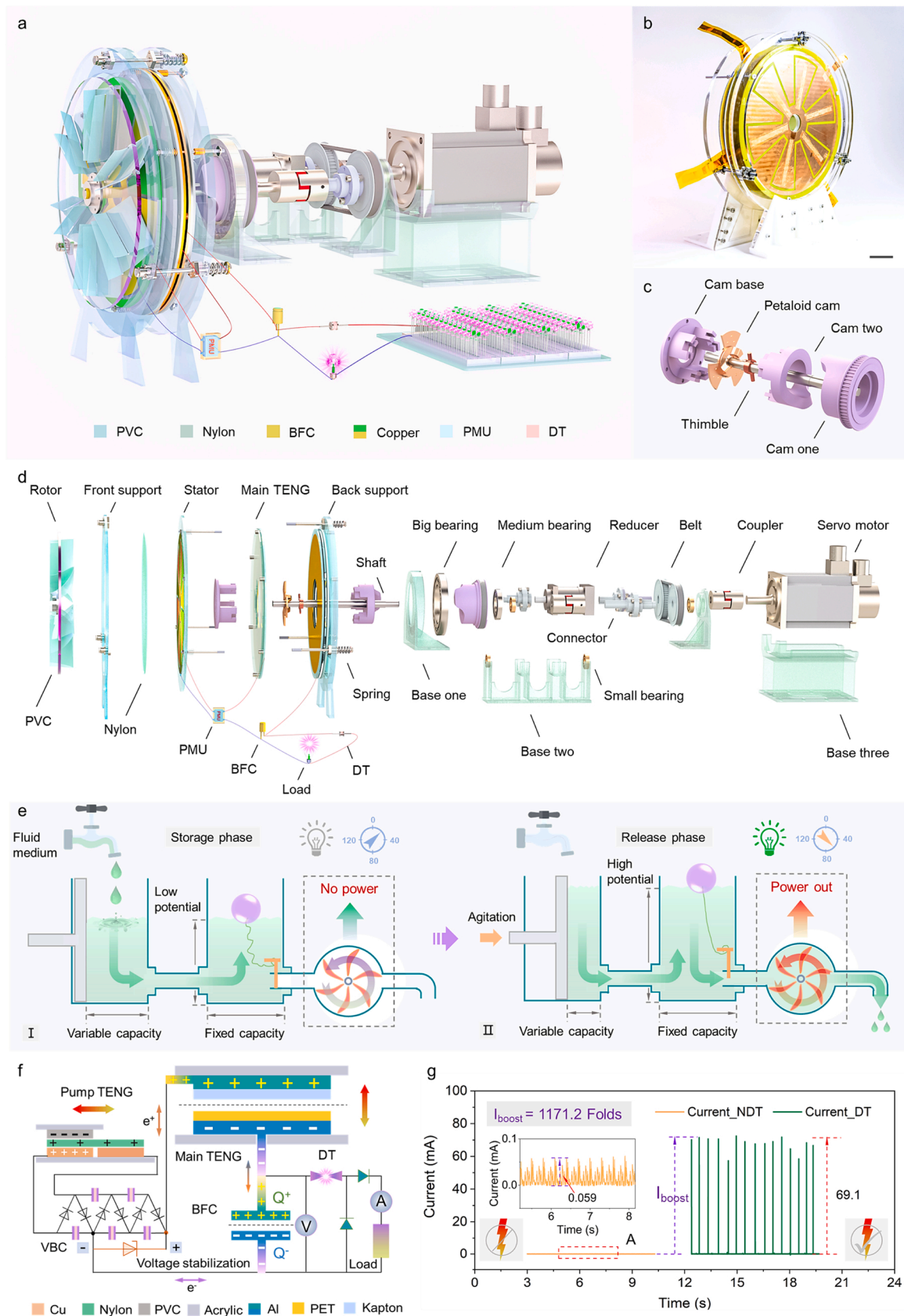


Fig. 1. Device structure and working principle of DCP-TENG. (a) Three-dimensional structure and components of DCP-TENG. Input voltage is rectified by a power management unit (PMU) to be imposed on main TENG and the buffer capacitor (BFC) in series. Electricity can be outputted through a discharge tube (DT). (b) Photograph of the electricity generation unit without a rotor (scale bar, 50 mm). (c) Structures of key components for the different movements of pump and main TENGs. (d) Structure components of DCP-TENG in explosive view. (e) Analogical mode based on a hydropower turbine for the work process of DCP-TENG. (f) Working principle of DCP-TENG. (g) Output currents of DCP-TENG with and without a DT.

voltage stabilization. In addition, the maximum capacitance is about 1.0 nF (0.98 nF) when the gap distance is only the total thickness of Kapton and PET films. As depicted in Fig. 1 g, the output current is of pulsed form with several high peaks when there is an incorporated DT, and the current (69.1 mA) with a DT is above 1000 times that (59 μ A) without a DT, indicating a great peak current enhancement with a DT.

2.2. Discharge tube and outputs of pump TENG and VBC

The schematic of DCP-TENG is shown in Fig. 2a. The working principle of a DT is that the current can flow through a DT only when its terminal voltage is higher than its breakdown voltage (V_{on}), or else the circuit is in disconnected state. The input AC voltage is rectified to a DC one (V_{DC}) by the VBC, which is imposed on the main TENG and BFC.

When the voltage of BFC is lower than V_{on} ($V_B < V_{on}$, I), the capacitance of main TENG increases along with the contact process of its

electrodes, improving its charge storage capacity. More positive and negative charges (e^+/e^-) will flow into one electrode of main TENG and BFC respectively, and equal charges with opposite signs occur on the other electrode of them due to the capacitor effect. The voltage of BFC is thus simultaneously on the increase, achieving an improving terminal potential between the DT through a diode. When the increasing V_B is higher than V_{on} ($V_B > V_{on}$, II), there is a current in circuit flowing through another diode and the load (R). Finally, the positive and negative charges (e^+/e^-) will flow back voltage source with the separation process of electrodes of main TENG, leading to a decreasing voltage on BFC and no potential difference between two terminals of the DT ($V_B < V_{on}$, III). In addition, there is a coupling effect of pumping charge and triboelectrification within main TENG, which promotes the charge storage on the surface of electrodes (Fig. S5).

Fig. 2b illustrates the charge distribution of pump TENG, induced by the coupling effects of triboelectrification and electrostatic induction.

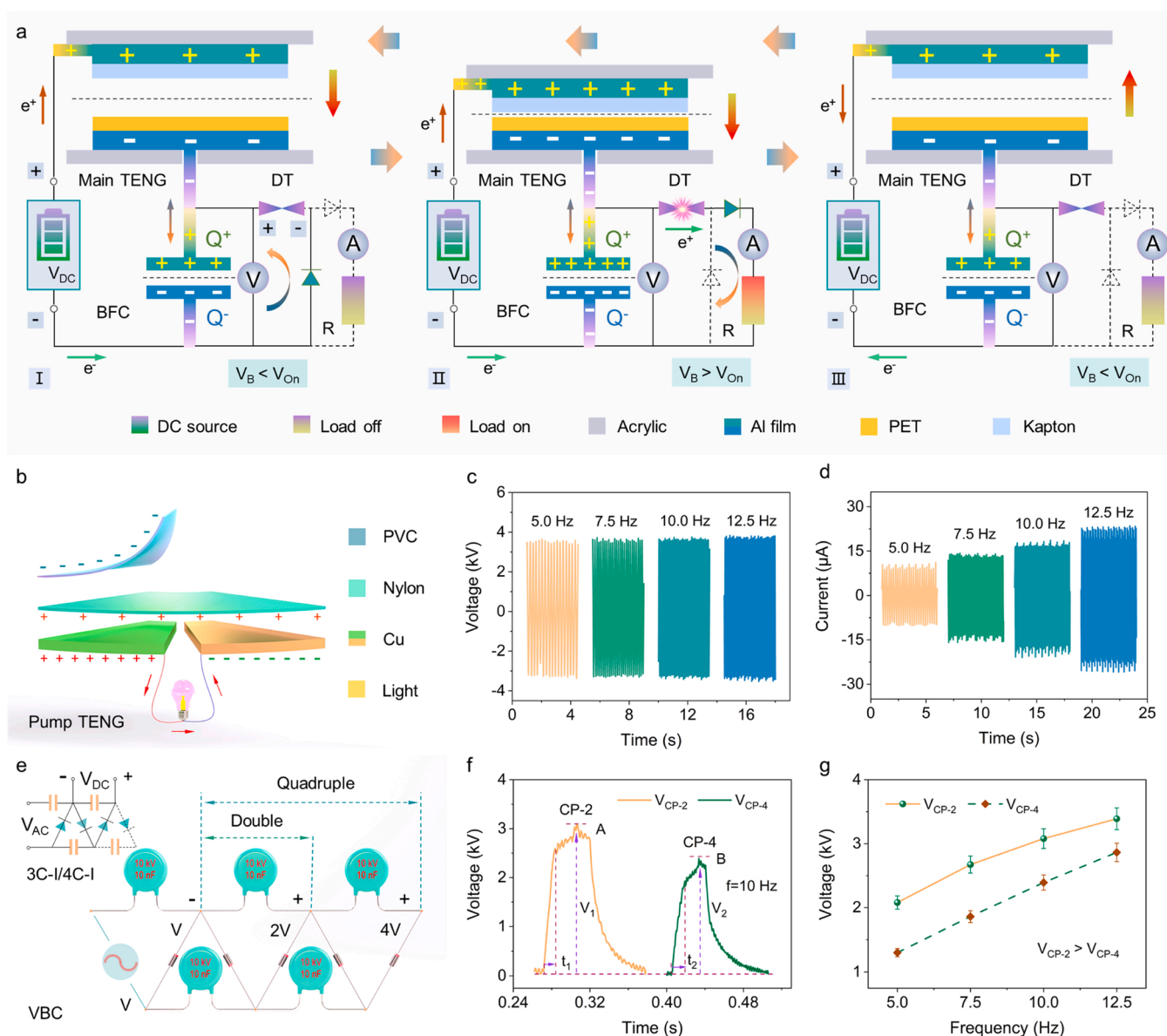


Fig. 2. Working process of DCP-TENG and outputs of pump TENG and VBC. (a) Working process of DCP-TENG. The current conduction in circuit depends on whether the V_B is higher than the breakdown voltage (V_{on}) or not. (b) Charge distribution of pump TENG based on the triboelectrification and electrostatic induction. (c) Open-circuit voltages of pump TENG under different driving frequencies. (d) Short-circuit currents of pump TENG under different driving frequencies. (e) VBC with five capacitors and diodes. The inset is the electric circuit of VBC in CP-2 mode. (f) Output voltages of VBC in CP-2 and CP-4 modes at 10.0 Hz. (g) Output voltages of VBC in CP-2 and CP-4 modes under different driving frequencies (10.0 Hz equals to 100 rpm).

When PVC film contacts nylon film and fully overlaps left electrode, there are negative charges building on PVC film due to its more negative triboelectricity than nylon film, leaving positive charges on nylon film with an equal amount. Owing to the electrostatic field effect between dielectrics, positive charges are induced on left copper electrode, while negative ones in equal quantity on right electrode. The potential difference between two electrodes produces current in conducting circuit, powering the lamp in Fig. 2b. The open-circuit voltage and short-circuit

current of pump TENG are both of alternating forms (Fig. 2c–d and Fig. S6a–b). With six sectors on one electrode of pump TENG, the current fluctuation frequency of 5.0 Hz corresponds to the rotation speed of 50 rpm from the servo motor (5.0 Hz equals to 50 rpm), and the 7.5 Hz, 10.0 Hz, and 12.5 Hz are thus to 75 rpm, 100 rpm, and 125 rpm, respectively. The open-circuit voltage nearly remains constant (about 3.6 kV) under different driving frequencies (Fig. 2c), while the short-circuit current linearly increases with the driving frequencies (Fig. 2d).

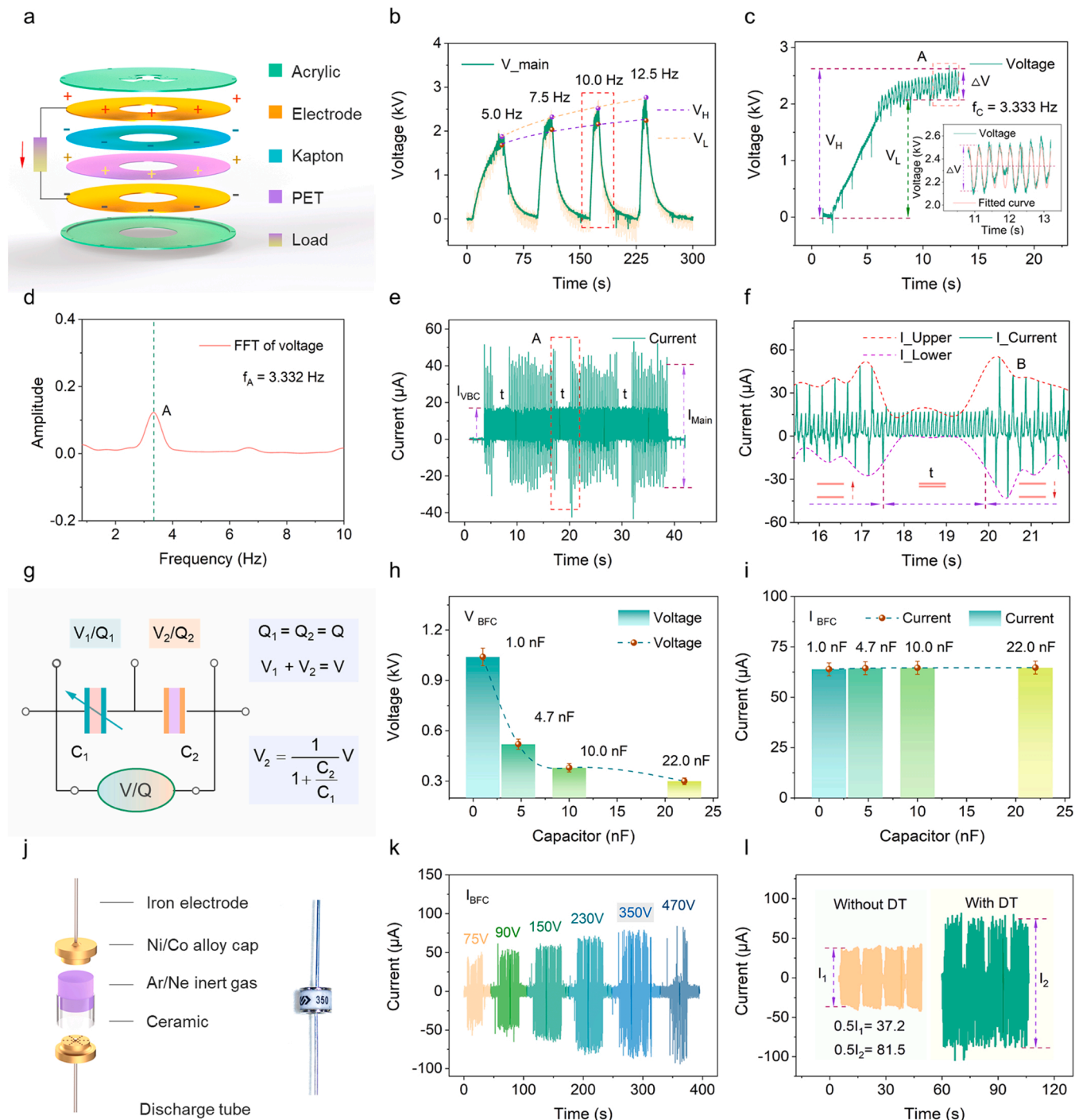


Fig. 3. Electric characteristics of Main TENG and BFC. (a) Structure and charge distribution of main TENG. (b) Output voltages of main TENG under different driving frequencies. (c) Output voltages of main TENG at 10.0 Hz (100 rpm). (d) Frequency spectrum curve of output voltage after the FFT. (e) Output current of main TENG by the superposition of I_{VBC} and I_{Main} . (f) Amplified current curve of dumbbell form. (g) Simplified and modeled schematic of main TENG and BFC in series. (h) Output voltages of BFCs with different capacitances. (i) Output currents of BFCs with different capacitances. (j) Structure of a DT and photograph of a commercial DT. (k) Output currents of BFC with different DTs. (l) Output currents of BFC with and without a DT.

A VBC, also named voltage-multiplying circuit (VMC) [42,50], consists of at least three diodes and capacitors with a special arrangement and it has a great scalability (Fig. 2e). The demanded AC voltage (V_{AC}) is rectified to the DC voltage (V_{DC}) by a VBC, theoretically outputting voltages with double (CP-2, 2 V), quadruple (CP-4, 4 V), etc., amplitudes of original one. The inset is the electrical circuit of VBC in CP-2 mode which has three or four capacitors (3 C-I/4 C-I). According to the fact that the capacitor with larger capacitance is charged with longer time and more electricity and the capacitance of capacitor would have little effect on the output voltage of VBC when its nominal voltage is two times bigger than the input voltage, the preferred capacitors within VBC are the ones of 10 kV/10 nF. In addition, it should be noted that the actual output of VBC is usually lower than the theoretical one on account of the parameter matches among its components.

Compared with CP-4 at 100 rpm (10.0 Hz), the voltage of CP-2 has a higher amplitude ($V_1 > V_2$) and a shorter charging time ($t_1 < t_2$) (Fig. 2f), which may be attributed to the incapability of pump TENG to provide high enough voltage and sufficient enough charges for a VBC with more capacitors. Meanwhile, output voltage of VBC increases with the driving frequencies and the CP-2 has higher ones than CP-4 ($V_{CP-2} > V_{CP-4}$) (Fig. 2g and Fig. S6c–d).

2.3. Electric characteristics of main TENG and BFC

The VBC has a more stable output voltage than that of the traditional full-bridge rectifier (FBR) and the VBC of 4 C-I is chosen as a rectifier because of its larger output current than that of 3 C-I (Fig. S7). Two electrodes of main TENG are both of ringlike and discoid shapes (Fig. 3a) and the PET and Kapton films serve as not only the tribo-layers but the protective films for separating them from each other and the air.

The output peak voltages (V_H , V_L) of main TENG increase with driving frequencies and the V_H and V_L are up to 2.6 kV and 2.1 kV at 100 rpm (10 Hz) (Fig. 3b). It has a small fluctuation (ΔV) of sinusoid form in steady state (inset in Fig. 3c), which is induced by the contact and separation of two electrodes. The charging process with an increasing voltage suggests the capacitor feature of main TENG. After the Fast Fourier Transform (FFT), the fundamental frequency (f_A in Fig. 3d) is 3.332 Hz equal to the projected 3.333 Hz, confirming the validity of measured datum.

When there is a close contact between two dielectrics, main TENG has no contact-separation movement but the maximum capacitance for the maximum charge storage. As shown in Fig. 3e, the output current is a superposition of one continuous part (I_{VBC}) from VBC and the other part (I_{Main}) from main TENG with an intermittent period (t). When amplified, the current curve A in Fig. 3e is of a dumbbell form with increasing and decreasing currents (I_{Main}) and there is no I_{Main} in the intermittent period (Figs. 3f and S8). Moreover, the flowing current between the pump TENG and main TENG is alternating and has a limited span due to the fact that the input voltage is constant and the distance between two electrodes is limited. The driving frequency has little effect on its amplitude but it will increase the total quantity of transfer charges with a faster one (Fig. S9).

The BFC is in series with main TENG, which can be simplified and modeled as the schematic in Fig. 3g. According to the series capacitor effect, the share rate of voltage of BFC (V_2) on the whole input voltage (V) depends on the ratio of C_2 (constant capacitance of BFC) and C_1 (variable capacitance of main TENG). With the constant C_2 , the V_2 is positively proportional to the C_1 . Meanwhile, the smaller the C_2 is, the bigger the V_2 is. Accordingly, the V_2 becomes the maximum one when the selected C_2 approaches the maximum C_1 (about 1.0 nF).

As shown in Fig. 3h–i, the V_{BFC} (V_2) decreases with the C_2 and becomes the maximum one when the C_2 is 1.0 nF while the I_{BFC} nearly remains constant, verifying the theoretical analysis. With the incorporated BFC, the output currents and voltages of BFC and main TENG are shown in Fig. S10. The DT works based on the gas discharge effect and its two metal electrodes switch from the open-circuit status into a

conducting one when its terminal voltage is high enough for the discharging of inert gases within it (Fig. 3j). The breakdown voltage of a DT is determined by the types and mixing ratio of inert gases. The actual dimension of main TENG and the common commercial DTs are shown in Fig. S11. Measured with the circuit in Fig. S12, the I_{BFC} increases with the breakdown voltage of a DT, while the DT of 350 V is finally chosen as the preferred one with a good discharging feature (Fig. 3k). The I_{BFC} with and without a DT are both alternating, while the one with a DT has a 2.2 folds enhancement from 74.4 μA (I_1) to 163 μA (I_2) (Fig. 3l).

2.4. Electricity output of DCP-TENG after rectified by FBRs

Two FBRs are incorporated into output circuits of main TENG and BFC respectively, converting AC currents into DC ones for powering the loads. The detailed output circuit of DCP-TENG is illustrated in Fig. S13. As shown in Fig. 4a, the total output current without DTs (I_{NDT}) is about 59.2 μA , which is within the limit (22 mA) of Keithley 6514 electrometer and can be directly measured. When there are DTs in DCP-TENG, the output current (I_{DT}) overflows the measurement range as shown in Fig. S14a–b. Based on the Ohm's law, the I_{DT} is calculated through dividing the measured voltage of a small resistor (load) by its resistance (10 Ω), resulting in the calculated current (69.1 mA) in Fig. 4b.

When integrating the amplified current curves (A, B) in Fig. 4a–b by the time, the accumulated charges (Q_1 , Q_2) within independent times (t_1 , t_2) are collected into Fig. 4c–d, respectively. Obviously, the DT has changed the output current into the one with a high instant pulse amplitude. As shown in Fig. 5e, the average charge quantity in one second with DTs (112.5 μC) is 8.041 folds of that (13.99 μC) without DTs, indicating a great charge enhancement of 704.1%. As the detailed deduction in Note S1, a charge density of 628.7 $\mu C m^{-2}$ is achieved. Moreover, the amplified single pulsed current without DT (A in Fig. 4c) has four peaks (P_1 – P_4 in Fig. 4f) and the output charge within 73.1 ms is 1.717 μC calculated through integrating the pulse current curve by the time (t). When incorporated with DT, the output current (B in Fig. 4d) has only one peak (P_1 in Fig. 4g) and the output charge within 1.38 ms is 31.997 μC . Therefore, the charge is outputted with a larger quantity and a higher efficiency with the discharge tube.

The total output current without DTs decreases with external loads due to the Ohmic loss and the maximum instantaneous peak power (P_A) is up to 115.9 mW, which is located at 1.0 G Ω (Fig. 4h). When DTs are incorporated into DCP-TENG, the output current also decreases with extra loads while the maximum instantaneous peak power (P_B , 313.6 W) is about 2700 folds of that (P_A) without DTs at the same external load [51–53] (R_B , 1.0 G Ω) (Fig. 4i). Moreover, the output currents of pump TENG, main TENG and the whole are collected in Fig. S14c–d, which are measured at 1.0 G Ω . Their effective values (average currents) at 1.0 G Ω are 3.15 μA (I_{rmsp}), 4.00 μA (I_{rmsm}), and 49.25 μA (I_{rmsw}), respectively, and the average powers of them are 9.92 mW ($I_{rmsp}^2 R_B$), 16.00 mW ($I_{rmsm}^2 R_B$), and 2.43 W ($I_{rmsw}^2 R_B$), respectively, and the average power densities of them are thus 163.7 mW/m², 297.8 mW/m², and 21.25 W/m², respectively.

2.5. Output circuit and applications of DCP-TENG with DTs

As shown in Fig. 5a, the DCP-TENG can produce electricity in two forms of pulsed and constant modes, which is realized by the different conducting combinations of a common switch with two connection terminals (point A and B). The load (R) and capacitor (C) are only used as the symbols for the electrical appliances, which do not have practical significance. After rectified by FBRs, the currents and voltages from main TENG and BFC are gathered in output terminals of DCP-TENG. When the point A is connected within the switch, the output pulsed current will directly pass through and power load (R), while it will firstly be stored in a capacitor (C) and then continuously powers the load when point B is connected within the switch. The effective value of current (I_{rms}) with DT that is measured at 1 G Ω , has a 12.2 folds increase

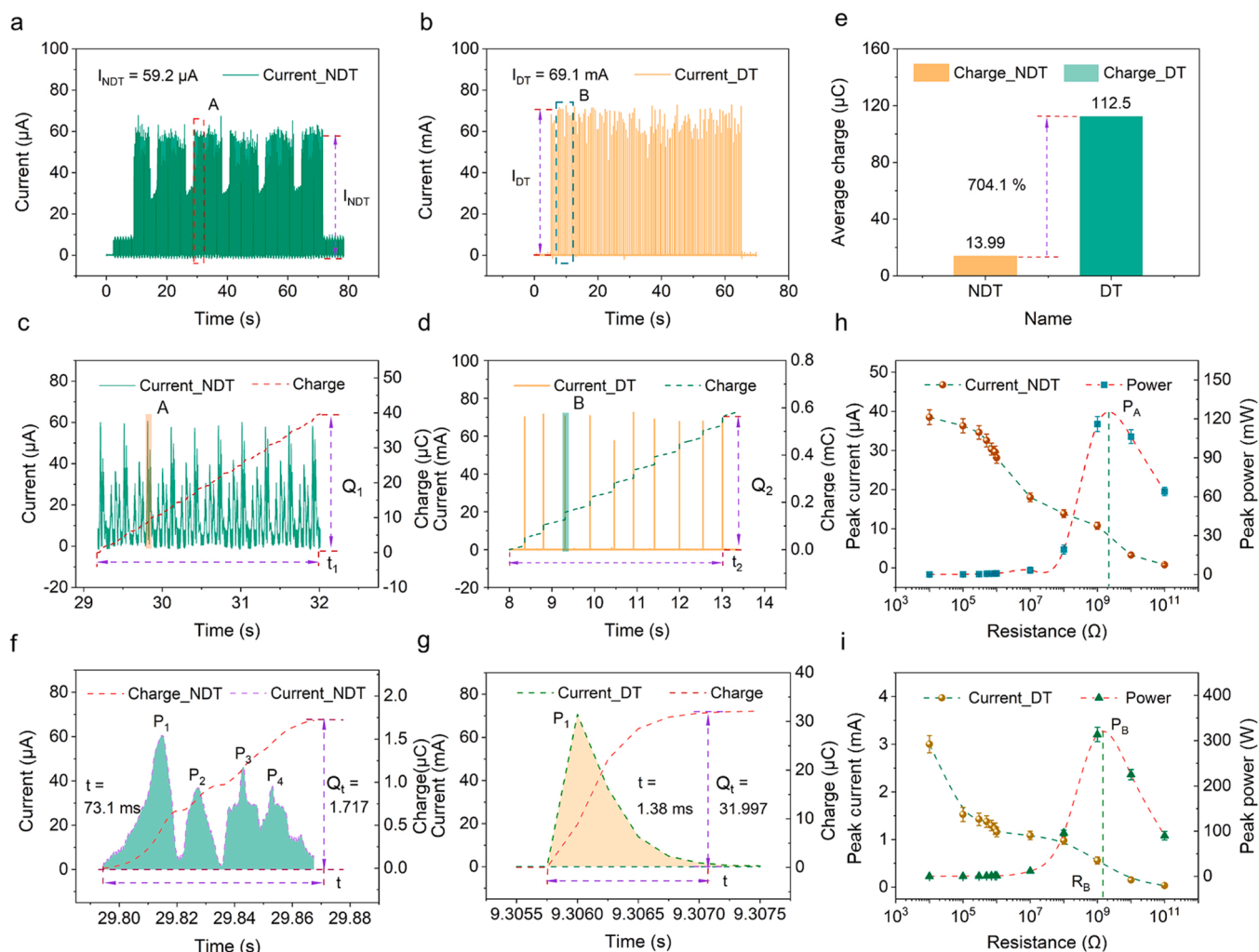


Fig. 4. Output electricity of DCP-TENG after rectified by FBRs. (a) Output current with DTs. (b) Output current without DTs. (c) Amplified current curve and accumulated charge without DTs. (d) Amplified current curve and accumulated charge with DTs. (e) Average charges in one second with and without DTs. (f) Single pulsed current curve without DT and its integrated charge curve. (g) Single pulsed current curve with DT and its integrated charge curve. (h) Peak current and power curves without DTs. (i) Peak current and power curves with DTs.

compared to that without DT (Fig. 5b) and the output peak power with DT has a great improvement than that without DT (Fig. 5c).

Adopting the constant mode of electricity output, the capacitor (470 μF) is charged to the working voltage of 3.2 V (V_1) within 162 s (t_1) when powering three electronic watches in series, and the V_1 decreases to 2.9 V (V_{11}) at a slow speed (211 s, t_{11}) (Fig. 5d). The capacitor (1000 μF) is charged to the working voltage of 1.8 V (V_2) within 293 s (t_2), and the V_2 then sharply decreases to V_{22} (0.8 V) within 28 s when powering two low-watt electronic sensors (t_{22}) (Fig. 5e).

Fig. 5f–g are the photographs of working low-watt electronics such as the digital watches, sensors, powered by DCP-TENG (Video S2). Fig. 5h is the photograph of the whole system and the inset is the still-shot image of powered 454 big LEDs with the diameter of 10 mm (Figs. S15 and S16). Meanwhile, the intermittent contact and separation within DCP-TENG can synchronously reduce the wear and abrasion of pump and main TENGs. Moreover, the DCP-TENG has the good durability and longtime stability with nearly the same amplitudes of output current or voltage before and after the test (Fig. S17). Compared with that without DTs, the 211 big LEDs and 936 small LEDs can be both lighted with a brighter luminance by the DCP-TENG with DTs (Fig. 5i–l), indicating a remarkable output current and a current enhancement (Video S3). Moreover, the output voltage is also high enough to power

three ultraviolet tubes in series (Fig. 5m) for the visualization of fluorescent ink (Fig. 5n and Video S4). Therefore, the DCP-TENG utilizes the BFC and DT as the energy regulation electronics to change the output energy form, transforming output current into the one with high instant pulse amplitude and boosting the instantaneous power.

Supplementary material related to this article can be found online at [doi:10.1016/j.nanoen.2022.107264](https://doi.org/10.1016/j.nanoen.2022.107264).

3. Conclusions

A new operation method of decoupled charge pump for TENG (DCP-TENG) along with the discharge tube is proposed to thousandfold improve its instantaneous peak current. The DCP-TENG adopts pump and main TENGs in freestanding triboelectric-layer and contact-separation modes and innovatively decouples their synchronous motions, maximizing the charge injection and storage when the capacitance of main TENG reaches the peak value. A voltage booster circuit are utilized to rectify the input current from pump TENG and a buffer capacitor for the charge storage. A cam mechanism is utilized to realize an intermittent contact and friction of dielectrics, reducing the abrasion. With the discharge tube, the output current has an above 1000 folds increase and the output average power is calculated to 2.43 W with

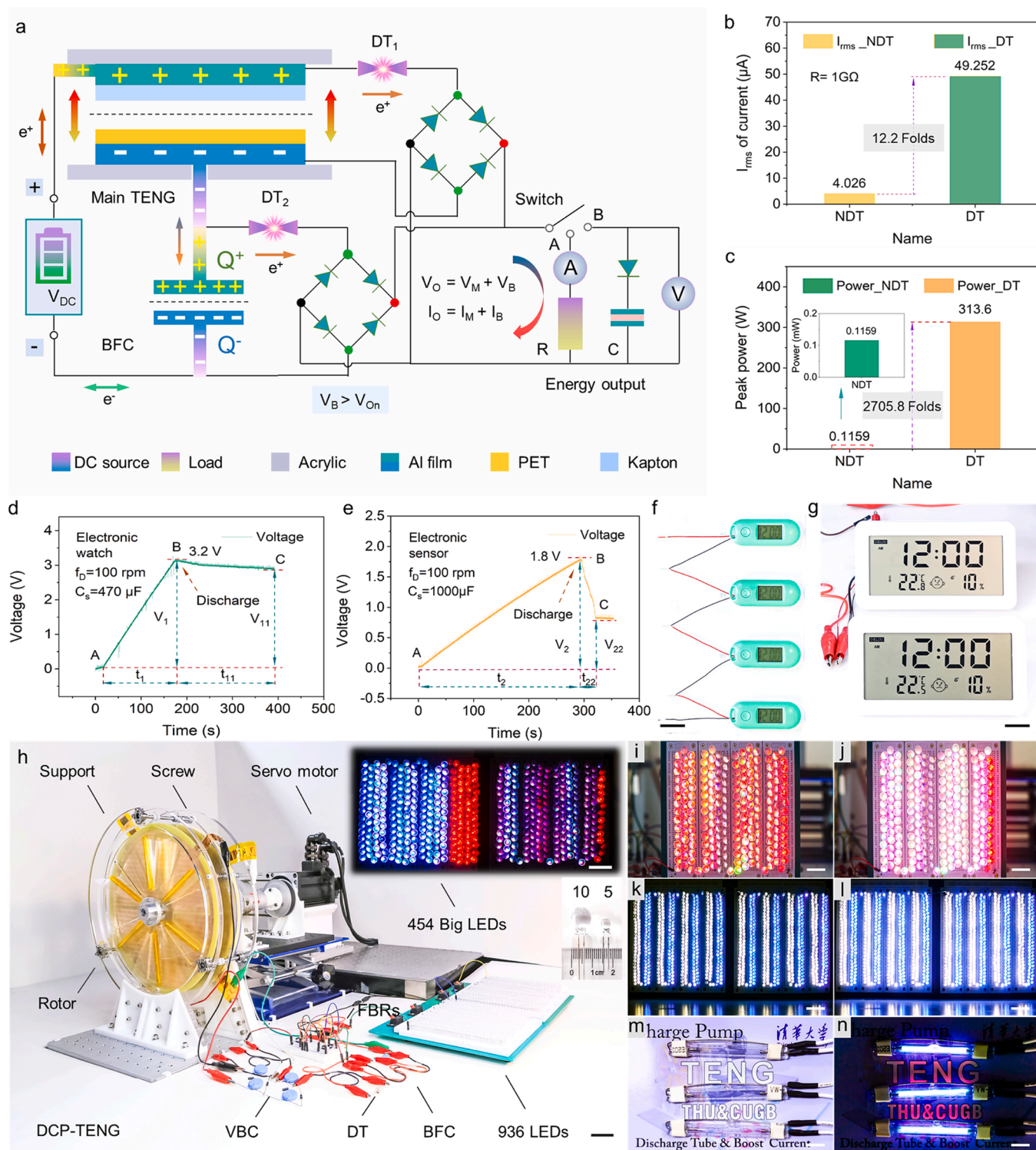


Fig. 5. Output circuit and applications of DCP-TENG with DTs. (a) Output circuit of DCP-TENG with DTs. (b) I_{rms} of current at 1 GΩ. (c) Output peak powers with and without DTs. (d) Charging and discharging curve of capacitor (470 μF/50 V). (e) Charging and discharging curve of capacitor (1000 μF/50 V). (f) Photograph of the working electronic watches (scale bar, 30 mm). (g) Photograph of the working sensors (scale bar, 30 mm). (h) Photograph of the DCP-TENG. The inset is the still-shot image of powered 454 big LEDs (scale bar, 50 mm). (i) Still-shot image of lighted 936 small LEDs without DTs. (j) Still-shot image of lighted 936 small LEDs with DTs. (k) Still-shot image of lighted 211 big LEDs without DTs. (l) Still-shot image of lighted 211 big LEDs with DTs (scale bar, 50 mm). (m) Photograph of unlighted ultraviolet tubes. (n) Still-shot image of lighted ultraviolet tubes (scale bar, 30 mm).

a power density of 21.25 W/m². Moreover, a charge density of 628.7 μC m⁻² is achieved. This work presents a new mode of decoupled charge pump with less abrasion, realizing the charge injection, storage and

transport with high efficiency. It could be regarded as a new approach for the great improvement of the output current of TENG, promoting its practical applications.

4. Methods and materials

4.1. Fabrication of pump TENG

The pump TENG was a rotatory TENG in freestanding triboelectric-layer mode, which mainly consisted of a rotator, a stator, one nylon layer, and six sectorial PVC films. The annular acrylic stator of $350 \times 35 \times 4$ mm served as the base of printed circuit board (PCB) substrate ($290 \times 35 \times 1$ mm) with metal electrodes. Two grid-shaped copper electrodes of 0.035 mm in thickness with a gap spacing of 5 mm were made by metal coating technology and formed on an annular PCB substrate. They both had six sectors with the same central angle of 60° . An annular nylon layer of $290 \times 35 \times 0.05$ mm was adhered to surfaces of electrodes using double-sided tapes. The circular rotator of $280 \times 280 \times 5$ mm was an acrylic disc with six rectangular through holes of 85×2 mm. The PVC films of 0.1 mm in thickness were attached on rotator by Kapton tape, and one ends of them passed through the holes, free to float and slide on the nylon layer. All the acrylic plates were fabricated by a laser cutter (version CM-1309, The G.U.Eagle America. Inc., USA).

4.2. Fabrication of main TENG

The main TENG was in contact-separation mode with two annular plate electrodes, PET layer, Kapton layer, and two annular acrylic bases. Two annular aluminum electrodes of $280 \times 100 \times 0.035$ mm were made by metal coating technology on two PCB substrates of $290 \times 90 \times 1$ mm. PCB substrates were bolted on two annular acrylic bases of $290 \times 90 \times 4$ mm. The annular PET and Kapton layers of $290 \times 90 \times 0.05$ mm were adhered to surfaces of electrodes respectively for the isolation and triboelectrification.

4.3. Fabrication of transmission mechanism

The motion transferring unit was composed of two couplers, two synchronous belt wheels, a gear reducer, three connectors and five ball bearings. Two couples both had the external diameter of 35 mm and height of 65 mm. One synchronous belt wheel had two wheels with the same diameter of 80 mm and the other with different diameters of 50 mm and 100 mm, respectively. The reduction ratio of gear reducer was 10 and small, medium, and large bearings were 16002, 16007, and 16016 in Chinese standards. All bases were made by 3D printing with acrylonitrile butadiene styrene (ABS) material on a printer (version 3DP-25-4 F, The Tiertime. Inc., China).

4.4. Fabrication and integration of DCP-TENG

The front and back supports with an external diameter of 350 mm and a height of 390 mm were used as the supporting frames, which were connected by three long screws with springs. The stator was fixed on long screws and the cam base was bolted on the stator. One electrode of main TENG bolted with a petaloid cam could slide on three short screws, which were bolted on the stator with springs. The thimble was fixed on the rotating shaft, so is the rotator with a flange.

4.5. Electrical measurement of DCP-TENG

All the output currents in DCP-TENG were measured by a Keithley 6514 system electrometer (version Keithley 6514, impedance $>200 \text{ T}\Omega$, The Keithley. Inc., USA). The open-circuit voltages of pump and main TENGs, buffer capacitor (1.0 nF, 10 kV), and the capacitors (1000 μF and 470 μF) were obtained by the Keithley 6514 system electrometer with a high-voltage probe (version HVP-40, 1/1000, The Pintech. Inc., China). Moreover, the still-shot images of lighted LEDs, electronic watches, sensors and three lighted ultraviolet tubes were all photographed by a digital camera (version D700, The Nikon. Inc., Japan).

CRedit authorship contribution statement

Z.L.W., J.C. and L.J. supervised the project. Z.Y., Y.Y. and J.C. conceived the idea and designed the experimental part. B.L., Y.L., X.L. and J.Q.C. helped with the fabrication of device and the measurement of electricity. F.L. assisted with the data processing and curve drawing. Y. Y., C.W., and L.J. helped to design the whole scheme and describe the results. All authors contributed to the paper.

Declaration of Competing Interest

The authors declare that they have no known competing financial interests or personal relationships that could have appeared to influence the work reported in this paper.

Acknowledgements

This research was supported by National Natural Science Foundation of China (No. 52075286), National Key Research and Development Program of China (No. 2021YFB3200300), National Science and Technology Major Project of China (No. 2011ZX02403).

Appendix A. Supporting information

Supplementary data associated with this article can be found in the online version at [doi:10.1016/j.nanoen.2022.107264](https://doi.org/10.1016/j.nanoen.2022.107264).

References

- [1] K. Shafique, B.A. Khawaja, F. Sabir, S. Qazi, M. Mustaqim, Internet of things (IoT) for next-generation smart systems: a review of current challenges, future trends and prospects for emerging 5G-IoT scenarios, *IEEE Access* 8 (2020) 23022–23040.
- [2] S. Liu, Mobile sensor network and wearable devices application in athlete muscle and physical fitness image monitoring, *Microprocess. Microsyst.* 82 (2021), 103856.
- [3] C. Xu, Y. Song, M. Han, H. Zhang, Portable and wearable self-powered systems based on emerging energy harvesting technology, *Microsyst. Nanoeng.* 7 (2021) 25.
- [4] P. Sun, S. Jiang, Y. Huang, Nanogenerator as self-powered sensing microsystems for safety monitoring, *Nano Energy* 81 (2021), 105646.
- [5] X. Gao, X. Liu, R. He, M. Wang, W. Xie, N.P. Brandon, B. Wu, H. Ling, S. Yang, Designed high-performance lithium-ion battery electrodes using a novel hybrid model-data driven approach, *Energy Storage Mater.* 36 (2021) 435–458.
- [6] C. Zhao, Q. Sun, J. Luo, J. Liang, Y. Liu, L. Zhang, J. Wang, S. Deng, X. Lin, X. Yang, H. Huang, S. Zhao, L. Zhang, S. Lu, X. Sun, 3D porous garnet/gel polymer hybrid electrolyte for safe solid-state Li–O₂ batteries with long lifetimes, *Chem. Mater.* 32 (2020) 10113–10119.
- [7] I.M. Peters, C. Breyer, S.A. Jaffer, S. Kurtz, T. Reindl, R. Sinton, M. Vetter, The role of batteries in meeting the PV terawatt challenge, *Joule* 5 (2021) 1353–1370.
- [8] H. Ryu, H.J. Yoon, S.W. Kim, Hybrid energy harvesters: toward sustainable energy harvesting, *Adv. Mater.* 31 (2019), 1802898.
- [9] F. Taghizadeh-Hesary, N. Yoshino, Sustainable solutions for green financing and investment in renewable energy projects, *Energies* 13 (2020) 788.
- [10] Z.L. Wang, Triboelectric nanogenerator (TENG)-sparking an energy and sensor revolution, *Adv. Energy Mater.* 10 (2020), 2000137.
- [11] W.G. Kim, D.W. Kim, I.W. Tcho, J.K. Kim, M.S. Kim, Y.K. Choi, Triboelectric nanogenerator: structure, mechanism, and applications, *ACS Nano* 15 (2021) 258–287.
- [12] C. Wu, A.C. Wang, W. Ding, H. Guo, Z.L. Wang, Triboelectric nanogenerator: a foundation of the energy for the new era, *Adv. Energy Mater.* 9 (2019), 1802906.
- [13] Y. Zi, L. Lin, J. Wang, S. Wang, J. Chen, X. Fan, P.K. Yang, F. Yi, Z.L. Wang, Triboelectric-pyroelectric-piezoelectric hybrid cell for high-efficiency energy-harvesting and self-powered sensing, *Adv. Mater.* 27 (2015) 2340–2347.
- [14] J. Wang, S. Qian, J. Yu, Q. Zhang, Z. Yuan, S. Sang, X. Zhou, L. Sun, Flexible and wearable PDMS-based triboelectric nanogenerator for self-powered tactile sensing, *Nanomaterials* 9 (2019) 1304.
- [15] J. Luo, Z.L. Wang, Recent advances in triboelectric nanogenerator based self-charging power systems, *Energy Storage Mater.* 23 (2019) 617–628.
- [16] W. Ding, J. Zhou, J. Cheng, Z. Wang, H. Guo, C. Wu, S. Xu, Z. Wu, X. Xie, Z. L. Wang, TriboPump: a low-cost, hand-powered water disinfection system, *Adv. Energy Mater.* 9 (2019), 1901320.
- [17] H. Huo, F. Liu, Y. Luo, Q. Gu, Y. Liu, Z. Wang, R. Chen, L. Ji, Y. Lu, R. Yao, Triboelectric nanogenerators for electro-assisted cell printing, *Nano Energy* 67 (2020), 104150.
- [18] A. Yu, P. Jiang, Z.L. Wang, Nanogenerator as self-powered vibration sensor, *Nano Energy* 1 (2012) 418–423.

- [19] Z.L. Wang, On the first principle theory of nanogenerators from Maxwell's equations, *Nano Energy* 68 (2020), 104272.
- [20] Y. Zi, J. Wang, S. Wang, S. Li, Z. Wen, H. Guo, Z.L. Wang, Effective energy storage from a triboelectric nanogenerator, *Nat. Commun.* 7 (2016) 10987.
- [21] H. Wang, M. Zhang, Z. Yang, Z. Wang, X. Liu, Y. Lu, L. Ji, Z.L. Wang, J. Cheng, Energy from greenhouse plastic films, *Nano Energy* 89 (2021), 106328.
- [22] Z. Yang, Y. Yang, F. Liu, Z. Wang, Y. Li, J. Qiu, X. Xiao, Z. Li, Y. Lu, L. Ji, Z.L. Wang, J. Cheng, Power backpack for energy harvesting and reduced load impact, *ACS Nano* 15 (2021) 2611–2623.
- [23] H. Li, Y. Sun, Y. Su, R. Li, H. Jiang, Y. Xie, X. Ding, X. Wu, Y. Tang, Multi-scale metal mesh based triboelectric nanogenerator for mechanical energy harvesting and respiratory monitoring, *Nano Energy* 89 (2021), 106423.
- [24] Y. Zi, C. Wu, W. Ding, X. Wang, Y. Dai, J. Cheng, J. Wang, Z. Wang, Z.L. Wang, Field emission of electrons powered by a triboelectric nanogenerator, *Adv. Funct. Mater.* 28 (2018), 1800610.
- [25] J. Wang, C. Meng, Q. Gu, M.C. Tseng, S.T. Tang, H.S. Kwok, J. Cheng, Y. Zi, Normally transparent tribo-induced smart window, *ACS Nano* 14 (2020) 3630–3639.
- [26] H. Wang, J. Cheng, Z. Wang, L. Ji, Z.L. Wang, Triboelectric nanogenerators for human-health care, *Sci. Bull.* 66 (2020) 490–511.
- [27] P. Ma, H. Zhu, H. Lu, Y. Zeng, N. Zheng, Z.L. Wang, X. Cao, Design of biodegradable wheat-straw based triboelectric nanogenerator as self-powered sensor for wind detection, *Nano Energy* 86 (2021), 106032.
- [28] S. Kuang, X. Suo, P. Song, J. Luo, Instantaneous self-powered sensing system based on planar-structured rotary triboelectric nanogenerator, *Sensors* 21 (2021) 3741.
- [29] Y. Liu, B. Chen, W. Li, L. Zu, W. Tang, Z.L. Wang, Bioinspired triboelectric soft robot driven by mechanical energy, *Adv. Funct. Mater.* 31 (2021), 2104770.
- [30] X. Wei, Z. Zhao, C. Zhang, W. Yuan, Z. Wu, J. Wang, Z.L. Wang, All-weather droplet-based triboelectric nanogenerator for wave energy harvesting, *ACS Nano* 15 (2021) 13200–13208.
- [31] C. Zhang, L. He, L. Zhou, O. Yang, W. Yuan, X. Wei, Y. Liu, L. Lu, J. Wang, Z. L. Wang, Active resonance triboelectric nanogenerator for harvesting omnidirectional water-wave energy, *Joule* 5 (2021) 1613–1623.
- [32] X. Liang, T. Jiang, G. Liu, Y. Feng, C. Zhang, Z.L. Wang, Spherical triboelectric nanogenerator integrated with power management module for harvesting multidirectional water wave energy, *Energy Environ. Sci.* 13 (2020) 277–285.
- [33] J. Cheng, W. Ding, Y. Zi, Y. Lu, L. Ji, F. Liu, C. Wu, Z.L. Wang, Triboelectric microplasma powered by mechanical stimuli, *Nat. Commun.* 9 (2018) 1–11.
- [34] F. Liu, Y. Liu, Y. Lu, Z. Wang, Y. Shi, L. Ji, J. Cheng, Electrical analysis of triboelectric nanogenerator for high voltage applications exemplified by DBD microplasma, *Nano Energy* 56 (2019) 482–493.
- [35] Z. Wang, Y. Shi, F. Liu, H. Wang, X. Liu, R. Sun, Y. Lu, L. Ji, Z.L. Wang, J. Cheng, Distributed mobile ultraviolet light sources driven by ambient mechanical stimuli, *Nano Energy* 74 (2020), 104910.
- [36] Y. Liu, K. Wang, C. Wu, J.H. Park, Z. Lin, Y. Zhang, X. Zhou, T. Guo, T.W. Kim, Triboelectric-nanogenerator-inspired light-emitting diode-in-capacitors for flexible operation in high-voltage and wireless drive modes, *Nano Energy* 78 (2020), 105281.
- [37] Y. Bai, L. Xu, S. Lin, J. Luo, H. Qin, K. Han, Z.L. Wang, Charge pumping strategy for rotation and sliding type triboelectric nanogenerators, *Adv. Energy Mater.* 10 (2020), 2000605.
- [38] L. Long, W. Liu, Z. Wang, W. He, G. Li, Q. Tang, H. Guo, X. Pu, Y. Liu, C. Hu, High performance floating self-excited sliding triboelectric nanogenerator for micro mechanical energy harvesting, *Nat. Commun.* 12 (2021) 4689.
- [39] T. Zhou, L. Zhang, F. Xue, W. Tang, C. Zhang, Z.L. Wang, Multilayered electret films based triboelectric nanogenerator, *Nano Res.* 9 (2016) 1442–1451.
- [40] J. Wang, C. Wu, Y. Dai, Z. Zhao, A. Wang, T. Zhang, Z.L. Wang, Achieving ultrahigh triboelectric charge density for efficient energy harvesting, *Nat. Commun.* 8 (2017) 1–8.
- [41] L. Xu, T.Z. Bu, X.D. Yang, C. Zhang, Z.L. Wang, Ultrahigh charge density realized by charge pumping at ambient conditions for triboelectric nanogenerators, *Nano Energy* 49 (2018) 625–633.
- [42] W. Liu, Z. Wang, G. Wang, G. Liu, J. Chen, X. Pu, Y. Xi, X. Wang, H. Guo, C. Hu, Integrated charge excitation triboelectric nanogenerator, *Nat. Commun.* 10 (2019) 1–9.
- [43] H. Wang, L. Xu, Y. Bai, Z.L. Wang, Pumping up the charge density of a triboelectric nanogenerator by charge-shuttling, *Nat. Commun.* 11 (2020) 1–9.
- [44] Z. Yang, Y. Yang, H. Wang, F. Liu, Y. Lu, L. Ji, Z.L. Wang, J. Cheng, Charge pumping for sliding-mode triboelectric nanogenerator with voltage stabilization and boosted current, *Adv. Energy Mater.* 11 (2021), 2101147.
- [45] S. Li, S. Wang, Y. Zi, Z. Wen, L. Lin, G. Zhang, Z.L. Wang, Largely improving the robustness and lifetime of triboelectric nanogenerators through automatic transition between contact and noncontact working states, *ACS Nano* 9 (2015) 7479–7487.
- [46] Z. Lin, B. Zhang, H. Zou, Z. Wu, H. Guo, Y. Zhang, J. Yang, Z.L. Wang, Rationally designed rotation triboelectric nanogenerators with much extended lifetime and durability, *Nano Energy* 68 (2020), 104378.
- [47] Z. Lin, B. Zhang, Y. Xie, Z. Wu, J. Yang, Z.L. Wang, Elastic-connection and soft-contact triboelectric nanogenerator with superior durability and efficiency, *Adv. Funct. Mater.* 31 (2021), 2105237.
- [48] G. Cheng, H. Zheng, F. Yang, L. Zhao, M. Zheng, J. Yang, H. Qin, Z. Du, Z.L. Wang, Managing and maximizing the output power of a triboelectric nanogenerator by controlled tip-electrode air-discharging and application for UV sensing, *Nano Energy* 44 (2018) 208–216.

- [49] K. Zhao, G. Gu, Y. Zhang, B. Zhang, F. Yang, L. Zhao, M. Zheng, G. Cheng, Z. Du, The self-powered CO₂ gas sensor based on gas discharge induced by triboelectric nanogenerator, *Nano Energy* 53 (2018) 898–905.
- [50] X. Liang, T. Jiang, Y. Feng, P. Lu, J. An, Z.L. Wang, Triboelectric nanogenerator network integrated with charge excitation circuit for effective water wave energy harvesting, *Adv. Energy Mater.* 10 (2020), 2002123.
- [51] H. Qin, G. Gu, W. Shang, H. Luo, W. Zhang, P. Cui, B. Zhang, J. Guo, G. Cheng, Z. Du, A universal and passive power management circuit with high efficiency for pulsed triboelectric nanogenerator, *Nano Energy* 68 (2020), 104372.
- [52] W. Shang, G. Gu, W. Zhang, H. Luo, T. Wang, B. Zhang, J. Guo, P. Cui, F. Yang, G. Cheng, Z. Du, Rotational pulsed triboelectric nanogenerators integrated with synchronously triggered mechanical switches for high efficiency self-powered systems, *Nano Energy* 82 (2021), 105725.
- [53] H. Qin, G. Cheng, Y. Zi, G. Gu, B. Zhang, W. Shang, F. Yang, J. Yang, Z. Du, Z. L. Wang, High energy storage efficiency triboelectric nanogenerators with unidirectional switches and passive power management circuits, *Adv. Funct. Mater.* 28 (2018), 1805216.



Ze Yang received his B.S. and M.S. degrees in Mechanical Engineering from Hubei University of Arts and Science in 2015 and Beihua University in 2018, respectively. He is currently pursuing the Ph.D. degree in Geological Equipment Engineering & Mechanical Engineering with the China University of Geosciences (Beijing) and Tsinghua University. His main research interests include the mechanical energy harvesting based on triboelectric nanogenerator (TEENG), high voltage application of TEENG, and self-powered systems.



Yiyong Yang is a Professor and PhD supervisor at School of Engineering and Technology, China University of Geosciences (Beijing). Dr. Yang received his Ph.D. degree in 2004 from the Department of Precision Instruments and Mechanics, Tsinghua University. He has focused on the researches of the intelligence and biomechanics, robotics, geological equipment engineering for a long time. In recent years, his research interests also include the design theory of modern machinery, modeling and simulation of dynamic system, design and control of robot, intelligent vehicle technology.



Fan Liu received his B.S. degree from Beihang University in 2016 and M.S. from Tsinghua University in 2019, both majored in Mechanical Engineering. He is currently a Ph. D. candidate in the Department of Mechanical Engineering of Massachusetts Institute of Technology. His previous works include medical robotics, triboelectric nanogenerators, microplasma. He is now working on instrumentation regarding mechanics of tumors.



Bo Li received her B.S. degree in Mechanical Engineering from the China University of Geosciences (Beijing) in 2019. She is currently pursuing the M.S. degree in Mechanical Engineering with the China University of Geosciences (Beijing) and Tsinghua University. Her main research interests include triboelectric nanogenerator, micro plasma and power management circuit.



Yinbo Li received a B.S. degree in Mechanical Engineering from Chongqing University, Chongqing, China, in 2016 and the Ph.D. degree in Mechanical Engineering at Tsinghua University, Beijing, China, in 2021. He was a visiting scholar in the Philips endowed Chair for Medical Information Technology at RWTH Aachen University, Aachen, Germany, during May–November, 2019. His research interests include the development of assistive robotics such as the powered lower limb exoskeletons, compliant actuators and dynamic modeling of complex mechanical systems.



Linhong Ji is a Professor and PhD supervisor at Tsinghua University, and the Chairman of Specialty Committee for Rehabilitation Medicine Engineering of Chinese Association of Rehabilitation Medicine. Dr. Ji received his B.S. and M.S. degrees in Mechanical Engineering from Tsinghua University in 1985 and 1988, respectively, and the Ph.D. degree in Precision Engineering from the University of Tokyo in 1996. He devoted much of his life to the rehabilitation engineering for different disabled people. At present, his current interests also include the rehabilitation robotics, human-robot interaction, neural modulation, and human potential enhancement.



Xu Liu received his Bachelor degree in Welding Technology and Engineering from Harbin Institute of Technology in 2019. He is currently pursuing the master degree in Mechanical Engineering in Tsinghua University. His main research interests include triboelectric nanogenerator and energy harvesting.



Zhong Lin Wang is the Chief scientist and Director for the Beijing Institute of Nanoenergy and Nanosystems, Chinese Academy of Sciences. Dr. Z. L. Wang also works as a Hightower Chair and Regents's Professor at Georgia Tech, and received his Ph.D. degree in Physics from Arizona State University. He has made lots of original and innovative discoveries and obtained many great achievements within the energy sciences, electronics, and optoelectronics. Owing to his important contributions in physical sciences, he won many famous scientific awards including the Albert Einstein Award. His research interests include the nanogenerator based on triboelectrification, blue energy harvesting, self-powered nanosystems, human-

electronics interface and sensors.



Jiaqi Chen received his B.S. degrees in Mechanical Design and Automation from China University of Geosciences (Beijing) in 2018. He is currently pursuing the M.S. degree in Mechanical Engineering with the China University of Geosciences (Beijing). His main research interests include triboelectric nanogenerator, plasma pulse technology.



Jia Cheng is an Associate Professor in the Department of Mechanical Engineering at Tsinghua University. He earned both his B.E. and Ph.D. degrees at Tsinghua University in 2002 and 2008, respectively. From 2017 to 2018, he worked as a visiting scholar in the research group of Prof. Z. L. Wang at Georgia Tech. During his post-doctoral study, he won the awards of Young Scientists of NSFC and China Postdoctoral Science Foundation. His research spans areas including mechanical design, multi-physics field, coupled simulation, optimization design, low temperature plasma, triboelectric nanogenerator, micro/nano technology, and rehabilitation engineering.



Chengbiao Wang is a Professor and PhD supervisor at China University of Geosciences (Beijing), and the Foreign Academician of Russian Academy of Engineering. Dr. Wang received his Ph.D. degree in 1991 from the Department of Precision Instrument and Mechanics, Tsinghua University. He has focused on the researches of machinery design theory and surface strengthening technology of machine part for a long time. Recently, his research interests also include the processing technology and equipment development of different coatings used on the surface of machine part, such as the abrasion resistance coating, antifriction coating, decorative coating, and anticorrosive coating.